Degradation behaviour analysis and end-of-life prediction of lithium titanate oxide batteries

Soltani, Mahdi; Vilsen, Søren Byg; Stroe, Ana-Irina; Knap, Vaclav; Stroe, Daniel-Ioan

Published in:
Journal of Energy Storage

DOI (link to publication from Publisher):
10.1016/j.est.2023.107745

Publication date:
2023

Document Version
Publisher's PDF, also known as Version of record

Journal of Energy Storage 68 (2023) 107745

Contents lists available at ScienceDirect

Journal of Energy Storage

journal homepage: www.elsevier.com/locate/est

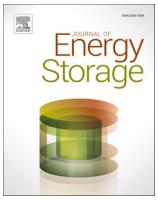

Research papers

Degradation behaviour analysis and end-of-life prediction of lithium titanate oxide batteries

Mahdi Soltani [a,*], Søren B. Vilsen [a,b], Ana-Irina Stroe [a,c], Vaclav Knap [d], Daniel-Ioan Stroe [a]

[a] Department of Energy, Aalborg University, Aalborg, Denmark
[b] Department of Mathematical Sciences, Aalborg University, Denmark
[c] KK Wind Solutions A/S, Ikast, Denmark
[d] Faculty of Electrical Engineering, Czech Technical University in Prague, 166 27 Prague, Czech Republic

ARTICLE INFO

Keywords:
Lithium titanate oxide
Cycling ageing
State of health
End of life
Feed forward neural network

ABSTRACT

Lithium-ion batteries (LiBs) with Lithium titanate oxide $Li_4Ti_5O_{12}$(LTO) negative electrodes are an alternative to graphite-based LiBs for high power applications. These cells offer a long lifetime, a wide operating temperature, and improved safety. To ensure the longevity and reliability of the LTO cells in different applications, battery health diagnosis, and lifetime prediction are crucial. This paper examines the cycling ageing behaviour of LTO cells in two different cell temperatures under high-current cycling conditions and various cycle depth (CD) tests. The ageing behaviour is investigated via capacity degradation trend using data-driven technique based on feed-forward neural network (FFNN). The model is later validated with the experimental result collected in-house and the lifetime data provided by the manufacturer. The proposed method accurately determines the state of health (SOH) level and predicts the end of life (EOL) with an acceptable error of 5 %.

1. Introduction

Electrochemical energy storage devices are widely used for portable, transportation, and stationary applications. Among the different types of energy storage devices on the market, lithium-ion batteries (LiBs) attract more attention due to their superior properties, including high energy density, high power density, and long cycle life [1]. The majority of LiBs are based on graphite anode materials, which have a high voltage and a high energy density; however, solid electrolyte interface formation (SEI) [2,3], and lithium plating are some of the drawbacks [4], which limit the battery life and might result in failures. The SEI formation is accelerated when using the graphite-based LiB at high current applications and/or at low temperatures [5]. To overcome this limitation, lithium titanate oxide (LTO) material is used as an alternative to graphite [6]. LTO is a spinel oxide, with a crystal structure which participates in Li + insertion–extraction processes [7]. This electrochemical process results in a structural change from spinel-LTO to rock-salt-LTO and corresponds to the voltage plateau at 1.55 V vs. Li+/Li. Moreover, this structure change tends to an almost negligible volume change of 0.2 % [8]. Therefore, LTO is known as a "zero-strain" material for Li + insertion [9]. In contrast, Li + insertion within graphite has a very low intercalation potential (~0.1 V vs. Li+/Li) [10] and causes a volume change of about ~10–13 % [11].

LTO negative electrode has several advantages over graphite, including, high mechanical stability, high-rate performance, and long cycle life. Moreover, the higher potential of the LTO electrode against Li results in a low cell voltage which effectively reduces the SEI formation, dendrites growth, and lithium plating [12,13]. However, the lower specific capacity (i.e., 150 Ah/kg) of the LTO electrode tends to lower specific energy of LTO cells (i.e., 74 Wh/kg) when compared to the graphite-based negative electrode, which is a challenge for some applications.

The positive electrode of a LTO cell are commonly made of lithium cobalt oxide (LCO), lithium–iron–phosphate (LFP), lithium–nickel–manganese–cobalt (NMC) oxide, lithium–manganese-oxide (LMO), and lithium–nickel–cobalt–aluminium (NCA) materials [14]. These chemistries all have their strengths and weaknesses, varying in energy and power density, toxicity, safety, and cost. In terms of ageing, the cathode is generally regarded as less significant [15]. The main ageing mechanisms of cathode materials include surface film formation, mechanical stress, and transition metal dissolution. Surface film formation (also known as cathode electrolyte interphase (CEI) layer) can form on the cathode, similar to the anode, but due to electrolyte oxidation and salt deposition [16]. In contrast to the SEI layer, the

* Corresponding author.
E-mail address: meh_soltani@yahoo.com (M. Soltani).

https://doi.org/10.1016/j.est.2023.107745
Received 15 September 2022; Received in revised form 10 May 2023; Accepted 15 May 2023
Available online 2 June 2023

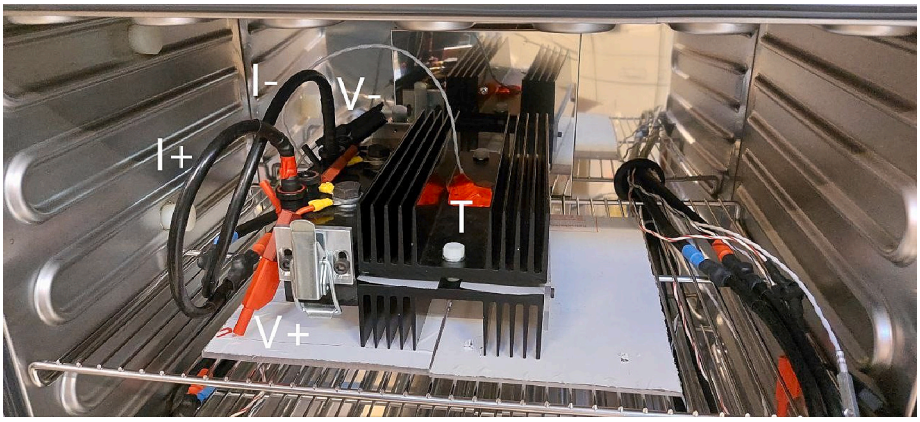

Fig. 1. Experimental set-up: LTO cell with the fixture placed in the oven and connected to the test channel.

Table 1
Electrical characteristics of the LTO/NMC battery cell.

Characteristics	Value
Nominal capacity	13 Ah
Nominal voltage	2.26 V
Maximum voltage	2.9 V
Minimum Voltage	1.5 V
Maximum charge/discharge current	130 A
Operating temperature	−40 °C to +50 °C
End of life	> 4000 FEC at 55 °C, 100 % cycle depth, 2C/2C

cathode surface layer shows low lithium-ion conductivity, increasing the impedance. Like the anode, the cathode can also undergo phase transitions during the intercalation and deintercalation of Li-ions, which can lead to a loss of active material and a loss of conductivity. Finally, structural degradation of cathode can happen due to the transition metal dissolution in the cathode.

In this research, the target is to examine the degradation behaviour of LTO cells in a fast response grid-scale battery energy storage system (BESS) with 1.2 MW/0.3 MWh specification for frequency regulation application for the Danish grid. LTO cell has been selected for this application due to its long cycle life and high-power capability. The high-power capability enables LTO cells to react rapidly to high power demands without having a negative impact on their lifetime. Although the cost of LTO cells in comparison to the graphite-based cells is higher, the price difference is moderated by calculating the price/cycle over the lifetime. To take the most advantage of LTO cells (long lifetime, high-rate capability, etc.) and ensure low price/cycle, a reliable lifetime estimation is needed.

Different perspectives for lifetime modelling have been presented in the literature [17]. For ageing analysis, some activities focus on an empirical approach and ageing test [18], while some others focus on post-mortem analysis [19]. Lifetime modelling based on an empirical approach is simple and accurate, including real-time and accelerated ageing tests. LTO batteries are known as a long-life energy storage system; therefore, lifetime testing under real-time tests is impractical. A large variety of research focused on the cycling ageing behaviour of LTO cells considering different stress factors, including, cycle depth, temperature, and current rates. Stroe et al. [20] compared two LTO cells at different degradation levels and different temperatures. The authors discussed the capacity evolution and internal resistance growth for two different test-cases. Liu et al. [21] analysed the cyclic ageing performance of LTO batteries at room temperature (RT). Their focus is on the degradation mechanism of LTO cells using incremental capacity and differential voltage techniques. Hall et al. [22] investigated the cycling behaviour of LTO cells at one temperature and different current rates. Nemeth et al. [23] studied the electro thermal properties and ageing behaviour of LTO cells for automotive applications. They studied the degradation behaviour at different temperatures but only at very high currents. Low and medium currents are neglected in this research. Stroe et al. [24] also presented a lifetime model for LTO cells based on the collected data by the time of publication. Bank et al. [25] analysed the ageing performance of LTO cells at different temperatures and cycle depths. Chahbaz et al. [26] studied calendar ageing and cyclic ageing mechanism for LTO cells using incremental capacity and differential voltage techniques. The authors have shown that the ageing rates vary as a function of SOC, temperature, DOD, and C-rate. Moreover, a two-stage ageing mechanism was determined by their result. In the first ageing stage, the anode is limiting the amount of extractable capacity. After a certain level of degradation is reached, the cathode starts limiting the amount of extractable capacity, initiating the second ageing stage with a stronger occurring capacity fading gradient. For most of the case studies presented above, the end of life has not been reached by the time of publication therefore, the lifetime model could not be validated properly.

In this research paper, different test-cases have been studied for ageing behaviour analysis considering the stress factors identified by Chahbaz et al. [26]. Tests have continued for four years to the end of life for most test-cases. Thanks to the long duration experimental data, an innovative state of health (SOH) estimation and end of life prediction model based on a feed-forward neural network (FFNN) modelling technique has been developed. The ageing analysis is based on an empirical approach which includes periodical capacity check-ups and accelerated ageing tests on LTO cells.

The remainder of this paper is structured as follows: Section 2 presents the experimental set-up. In Section 3, the result is presented and discussed. Section 4 focuses on the cells' lifetime modelling and validation. In Section 5, the conclusion and the key achievements are presented.

2. Experimental setup

2.1. Investigated cell

In this research work, high-power LTO battery cells with a pouch format as shown in Fig. 1 have been tested and analysed for lifetime modelling studies. The used battery is composed of LTO and NMC electrode materials for the anode and cathode, respectively. The battery cell specification has been presented in Table 1. The manufacturer's information and NMC materials composition have not been disclosed due to the non-disclosure agreement (NDA) with the manufacturer.

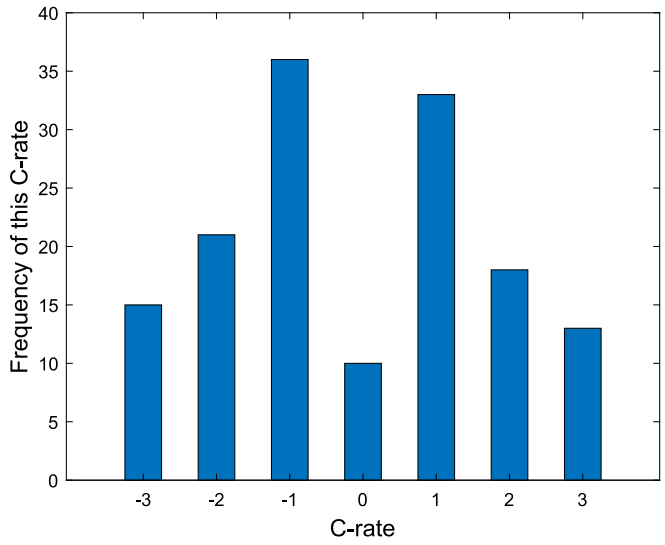

Fig. 2. Frequency distribution of different C-rates (charge/discharge) of the real-life load profile.

Table 2
Cycling ageing test matrix.

Test-case (TC)	Cell ID	Operating conditions-Stress factors		
		Current rate (ch/dch)	Cycle depth (%)	Cell temperature (°C)
Cycling TC1	Cell 1& Cell 2	2C/2C	10	50
Cycling TC2	Cell 3& Cell 4	1C/1C	50	50
Cycling TC3	Cell 5& Cell 6	2C/2C	50	50
Cycling TC4	Cell 7	2C/2C	10	42.5
Cycling TC5	Cell 10	2C/2C	30	42.5
Cycling TC6	Cell 12	1C/1C	50	42.5
Cycling TC7	Cell 13	2C/2C	50	42.5
Cycling TC8	Cell 16	3C/3C	50	42.5

2.2. Cycling ageing test

As mentioned earlier, the objective of this research is to investigate the degradation behaviour of LTO cells in a fast response grid scale BESS for frequency regulation application. According to the frequency regulation scheme of the target country, a closed loop control algorithm has been used to maximize the grid support and to extend the lifetime of BESS by reducing the number of cycles of the battery system. Based on the proposed algorithm, a maximum C-rate of 3C and an average current of C/2 were obtained for this application. The frequency distribution of the different C-rates of the real load profile is shown in Fig. 2. As can be seen in this figure, the current 3C is less frequent than the 2C and 1C. The temperature increase (ΔT) at 3C continuous cycling for a single cell is 13 °C and is less likely in real load profiles; however, in the interest of comprehensive modelling, high C-rates and high temperatures were considered in this study.

Initially, three test temperatures (35, 42.5, and 50 °C) were selected for accelerated ageing tests; however, due to a very slow degradation behaviour at 35 °C, the test was continued at 42.5, and 50 °C and the degradation result provided by the manufacturer at 25 °C is used as third temperature for modelling and model validation. The designed test matrix in this research consists of 16 LTO battery cells in eight different test-cases. As shown in Table 2, due to the performance failure of one

Table 3
Test set-up equipment specification.

Digatron BTS 600 battery testers	Memmert UNP 500 and Memmert UFP 600
Current range: −50 to +50 A Voltage range: 0 to 6 V Voltage accuracy 0.001 V Current accuracy: 0.01 A Temperature accuracy: 0.1 °C	Temperature range: 30 - 250 Temperature accuracy: 0.5°C below 99.9°C and 1°C above 100°C

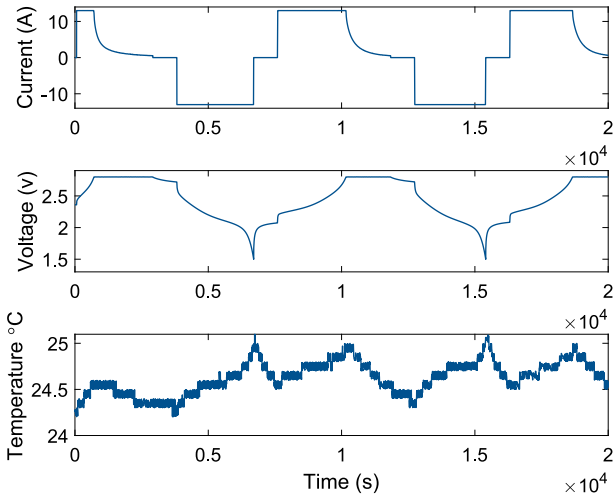

Fig. 4. A capacity measurement test for characterisation of LTO cell.

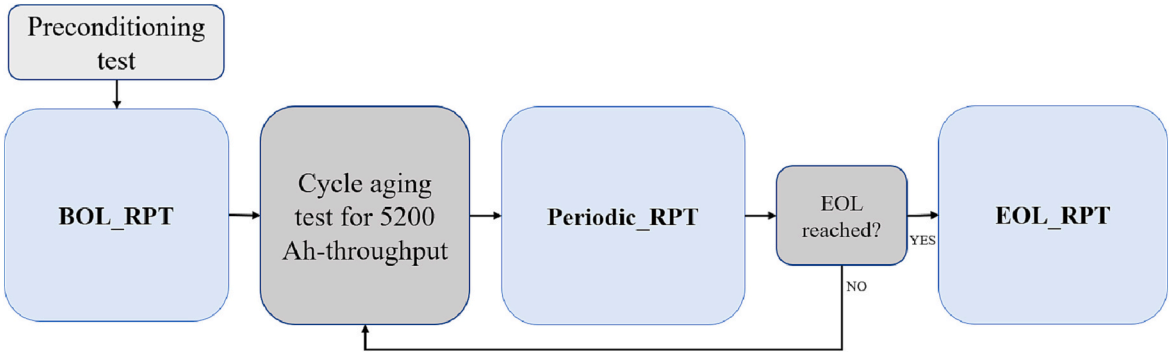

Fig. 3. Test methodology for cycle life test.

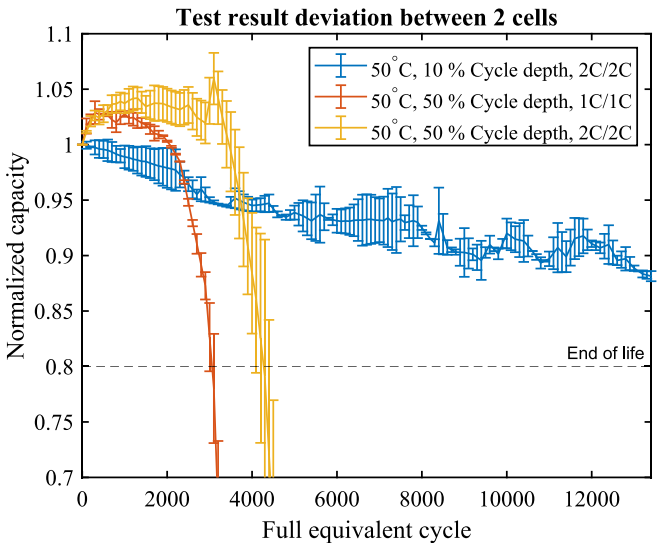

Fig. 5. Normalised capacity deviation between two cells of each test-case at 50 °C.

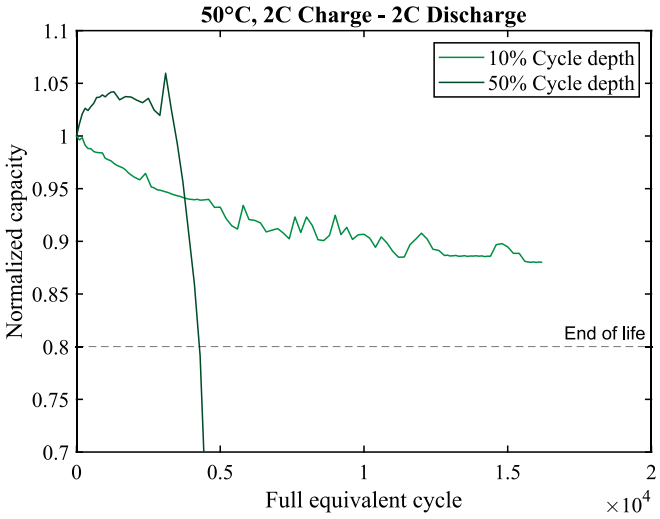

Fig. 8. Capacity degradation of cells aged at 2C charge/discharge current and 50 °C as a function of FEC for different cycle depths. (TC1/TC3).

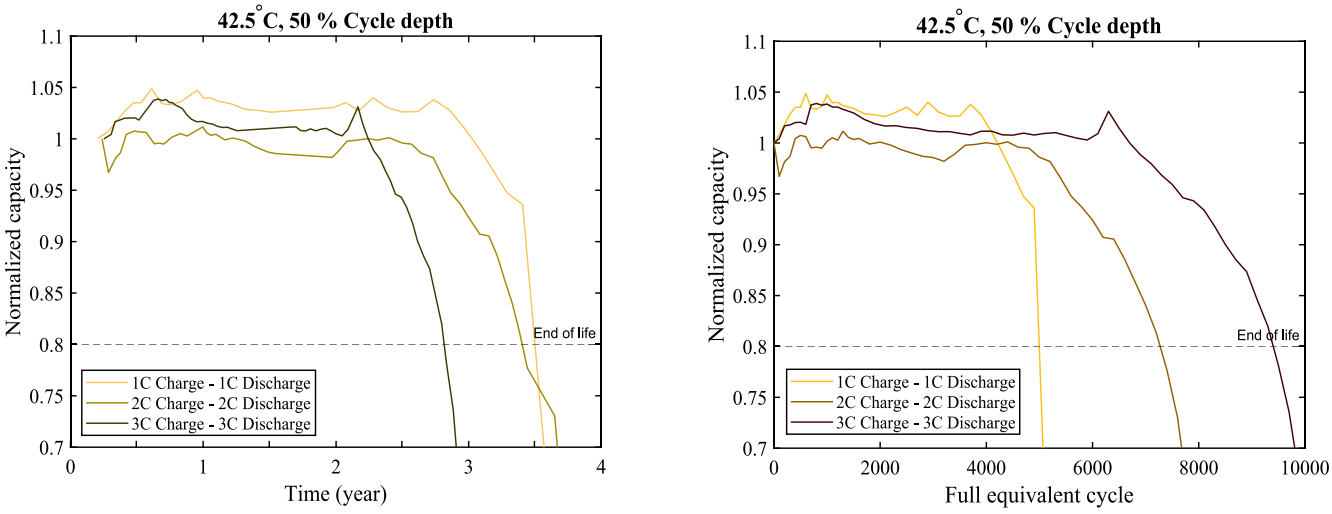

Fig. 6. Capacity evolution at 50 % cycle depth and 42.5 °C as a function of time (left) and FEC (right) for different C-rates (TC6/TC7/TC8).

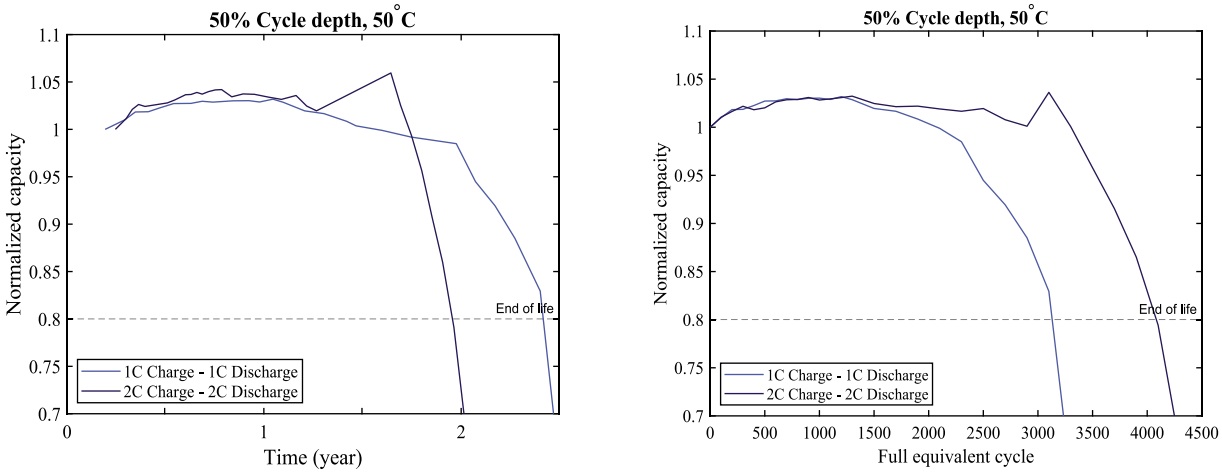

Fig. 7. Capacity evolution at 50 % cycle depth and 50 °C as a function of time (left) and FEC (right) for different C-rates (TC2/TC3).

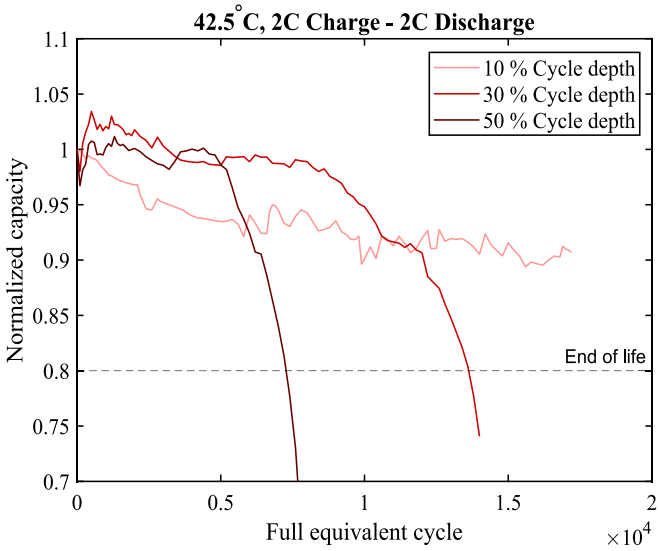

Fig. 9. Capacity degradation of cells aged at 2C charge/discharge current and 42.5 °C as a function of FEC for different cycle depths. (TC4/TC5/TC7).

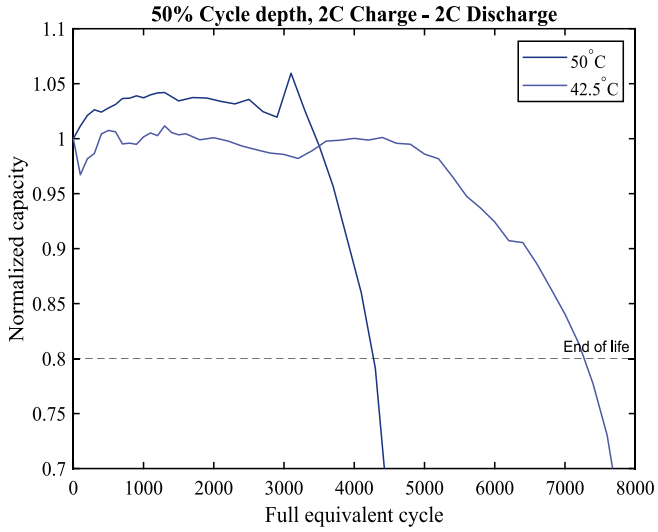

Fig. 10. Capacity evolution for 2C charge/discharge current and 50 % cycle depth as a function of FEC for different temperatures (TC3/TC7).

cell in test-cases 4 to 8, only one cell per these conditions has been studied. The cells were tested inside fixtures in order to maintain the volume constant during cycling. The experimental set up presented in Fig. 1 shows a battery cell mounted in a fixture, which is placed in an oven, and connected to the battery tester. The cells have been constrained according to the manufacturer's recommendation with two aluminium plates of 5 mm thickness under a total compression of 3.7 psi (22,258 Pa).

Stress factors influencing the cycle lifetime of the cells include temperature, current rate, and cycle depth. For all test-cases, the SOC is 50 % and the test temperature is the temperature measured on the surface of the cell.

Fig. 3 shows the cycle life test sequence from the beginning of life (BOL) to the end of life (EOL). First, a preconditioning test is performed according to IEC 62660–1 [27] to ensure the stabilisation of the cell. The test continues for 5 cycles at the current specified by the manufacturer, followed by 30 min of rest. After the preconditioning test, a reference performance test (RPT) is performed at BOL. Subsequently, the cells of the individual test-cases (TCs) are cycled according to the test conditions

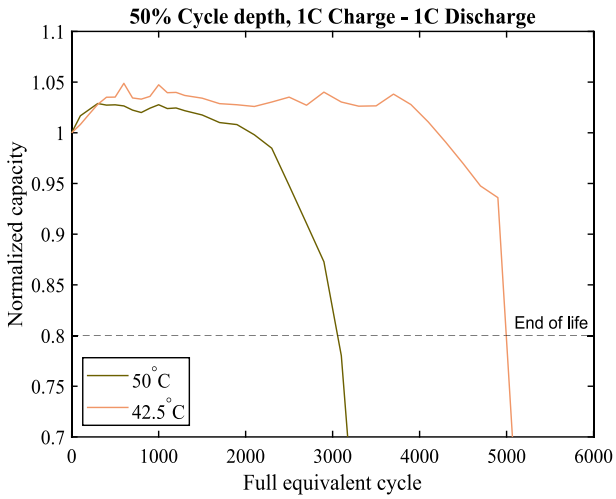

Fig. 11. Capacity evolution for 1C charge/discharge current and 50 % cycle depth as a function of FEC for different temperatures (TC2/TC6).

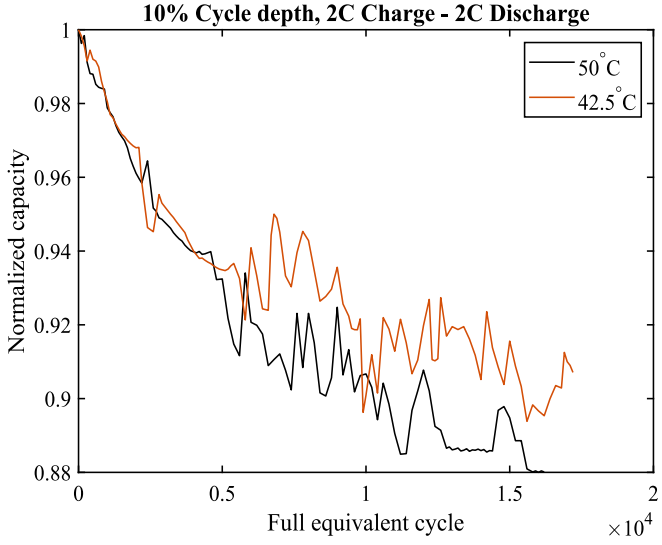

Fig. 12. Capacity evolution for 2C charge/discharge current and 10 % cycle depth as a function of FEC for different temperatures. (TC1/TC4).

Table 4
Theoretical boundaries for cyclic ageing model.

Parameter	Value
Cycle depth	50 % > CD >10 %
Mid SOC	SOC = 50 %
Temperature	50 °C > T > 42.5 °C
Current rate	3C > C-rate > 1C

explained in Table 2 before the periodic RPT is performed.

In order to analyse the actual state of the cells, the full equivalent cycle (FEC) is used to describe the total charge throughput of a cell. One FEC corresponds to one complete charge and one complete discharge over the rated capacity of the cell multiplied by two, as given in (1)

$$FEC = \frac{\int |I_{cycle}| . dt}{2C_{nom}} \quad (1)$$

where I_{cycle} is the current during a complete charge and discharge cycle and C_{nom} is the nominal capacity [28]. After each 5200 Ah throughput at

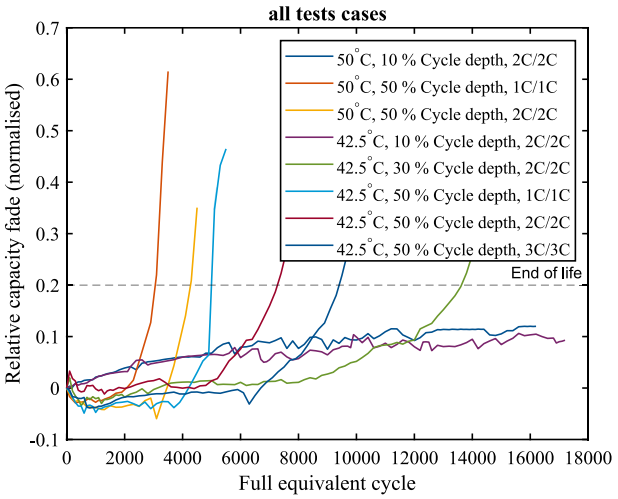

Fig. 13. The relative capacity fade as a function of FEC for different test-cases shown in Table 2.

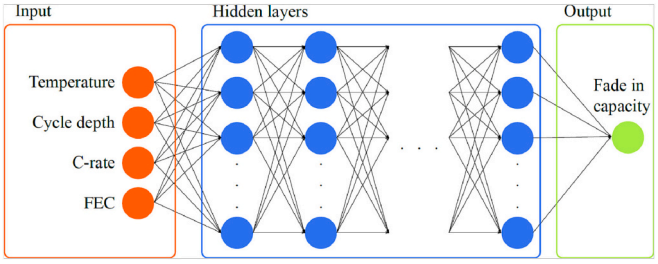

Fig. 14. General structure of a feed forward neural network.

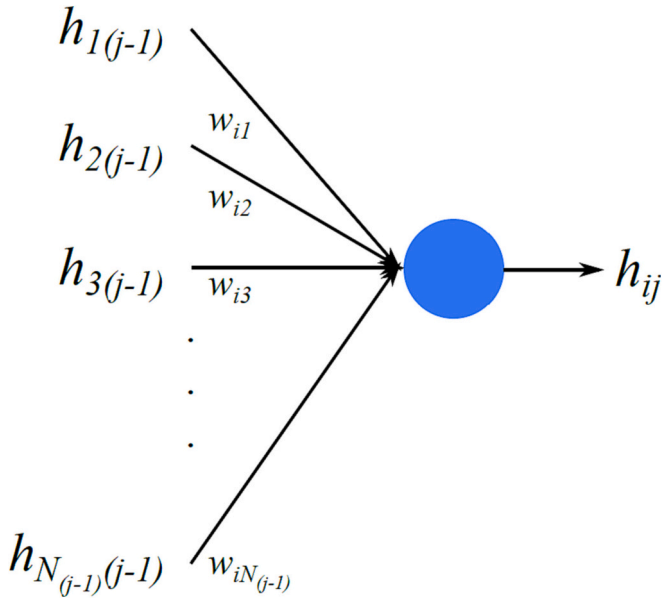

Fig. 15. General structure of a neuron in the FFNN.

test temperature, which corresponds to 200 FECs, a periodic RPT is performed at 25 °C. The periodic RPT is used to analyse the health of the cells for all test-cases listed in Table 2 and is discussed in detail in the next section. If the EOL has not yet been reached, the procedure is repeated, and when the EOL is reached, an EOL RPT is performed and the cycle life test is completed. The cycle life tests were performed using

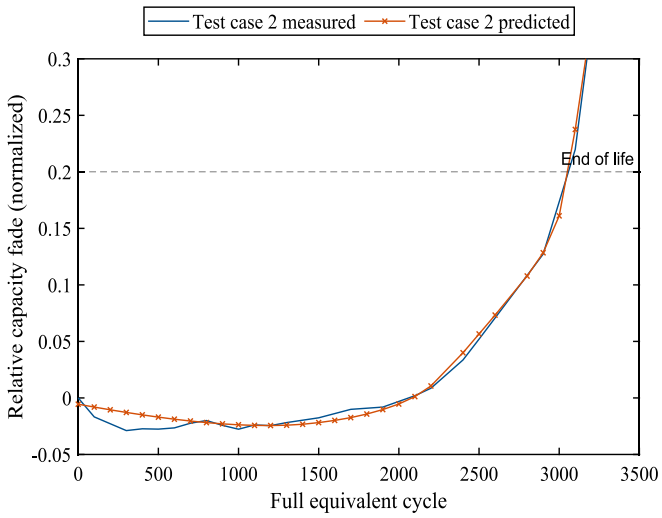

Fig. 16. Comparison between the experimental data and the predicted model for test- case 2 used for model training.

a Digatron BTS 600 battery tester. Memmert UNP 500 and Memmert UFP 600 temperature chambers were used to maintain temperature during ageing and RPT tests. The equipment characteristics are listed in Table 3.

2.3. Reference performance test

RPT in this study is a capacity measurement test. Capacity measurement is performed after every 200 FECs as explained in the previous section. Initially, the capacity measurement test was performed every 100 FEC; however, due to a small variation in capacity, a periodic check was performed every 200 FECs.

2.3.1. Capacity measurement

Capacity measurement is performed on a fully charged cell in two steps: constant current at 1C and constant voltage at 2.8 V with $0.04 \times I_n$ limiting current. After a 15 min rest period, the cell is discharged at 1C to the end-of-discharge voltage (1.5 V). For statistical analysis, two capacity measurements are performed, and the second discharging capacity measurement is used in the analysis. The current, voltage, and temperature signals during a RPT are shown in Fig. 4.

3. Results and discussion

3.1. Capacity fade

To further investigate the capacity evolution over the lifetime, different stress factors were investigated, as explained in Table 2. For a better comparison, all values were normalised using (2) to a reference value measured at the beginning of life under the respective test conditions.

$$Normalised\ capacity\ [\%] = \frac{Capacity_{actual}}{Capacity_{BOL}} \times 100\% \quad (2)$$

where $Capacity_{actual}$ is the measured value at test condition, and $Capacity_{BOL}$ is the initial capacity at the beginning of life at test condition. As explained in Table 2, there are two battery cells per test-case. The average capacity of the two cells in each test-case is used for lifetime modelling unless there is only one cell for a test-case due to cell failure. The test result deviation between two cells of each test-case at 50 °C is shown in Fig. 5.

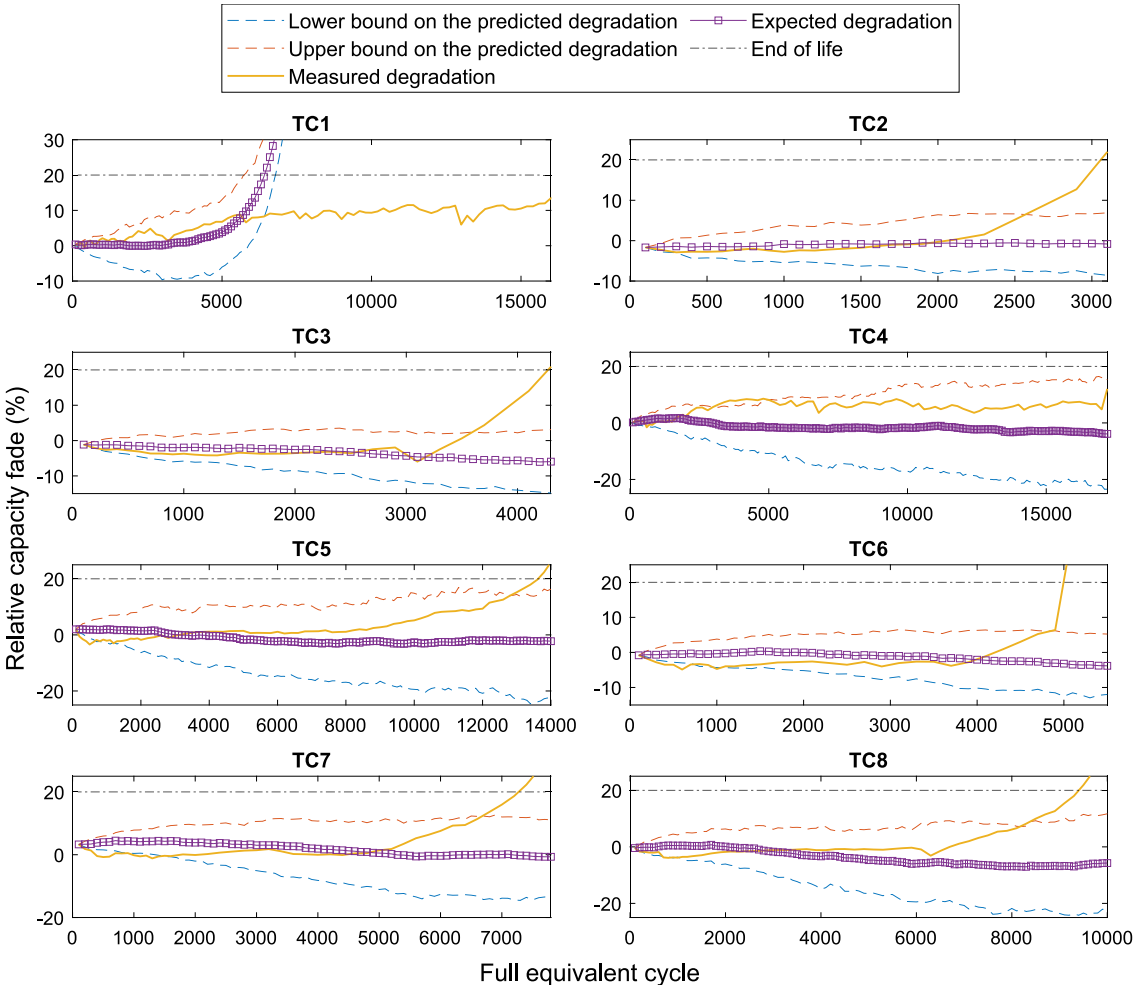

Fig. 17. The predicted capacity fade as a function of FEC, without having any experimental result for each test-case.

3.1.1. *Influence of C-rate*

In Fig. 6, the influence of C-rate on the capacity degradation at 42.5 °C is presented as a function of FECs and time. As can be seen, the cells cycled with a higher C-rate show a longer cycle life; however, these cells degrade faster in a shorter time. This can be explained by the impact of calendar life on degradation. A cell cycled at a low C-rate will be imposed to the high temperature for a longer time; therefore, it is degraded faster in terms of the FEC number. The result presented in Fig. 6 reveals that the cells cycled with 1C/1C charge/discharge profile reached the end of life after 5000 FEC in 39.5 months. In this test condition, the cells can withstand 1519 FECs/year before reaching the EOL criterion. The cells cycled at 2C/2C can withstand 7000 FECs, in 37 months, before reaching the EOL criterion. This is equal to 2270 FECs/year. The cells cycled at 3C/3C can perform 9400 cycles in about 30 months before reaching the EOL which is equal to 3760 FEC/year. A higher number of cycles at higher C-rates is observed but at a shorter time. The battery can also perform 60, 400, and 400 FECs between 80 % and 70 % SOH for 1C/1C, 2C/2C, and 3C/3C test profiles, respectively.

A similar result is seen when comparing the capacity fade result for the cells cycled at 50 °C. As shown in Fig. 7, cells cycled at 2C/2C have a 33 % longer cycle life than 1C/1C test profile; however, in terms of the required time to reach the end of life, it is 23 % shorter.

3.1.2. *Influence of cycle depth*

Another influencing factor on the capacity degradation, as shown in Figs. 8 and 9, is the cycle depth. As can be seen from these figures, the cell cycled with a lower cycle depth for a similar temperature and current, has a longer cycle life; for example, after 16,000 FEC, <15 % capacity fade is observed. Independent of temperature and C-rate, for 30 % and 50 % cycle depth cases, the capacity fade curves show three stages: capacity increase, very slow capacity decrease, and abrupt capacity fade.

The capacity increase stage can be because of the increased electrode active surface area as a result of electrochemical milling [29]. Similar behaviour for LTO cells has been reported by Nemeth et al. [23], where LTO cells investigated at two different ambient temperatures have shown the three stages mentioned above at 45 °C and 100 % cycle depth. The abrupt capacity drop in the third ageing stage has been reported at high cell temperature (55 °C) corresponding to the high internal resistance. It can be observed that the cells cycled at 10 % cycle depth only comprise a slow capacity fade stage. Therefore, at the beginning of the test, these cells degrade faster than those with high cycle depth; however, after the abrupt capacity fade stage for cells with high cycle depth, the trend is reversed. It can be concluded that the LTO cells show high cyclic stability, especially when cycled at low cycle depth. A similar result has been reported by Chahbaz et al. [26]. The authors have shown that cyclic ageing at high cycle depths is accelerated, and the fastest ageing happens at 100 % cycle depth. Bank et al. [25] reported a slow-rate capacity degradation for small cycle depth load profiles. The finding in this research paper agrees with the results of various studies performed on other types of LIBs [30].

3.1.3. *Influence of temperature*

The effect of temperature on LTO cell cycle life are shown in Figs. 10

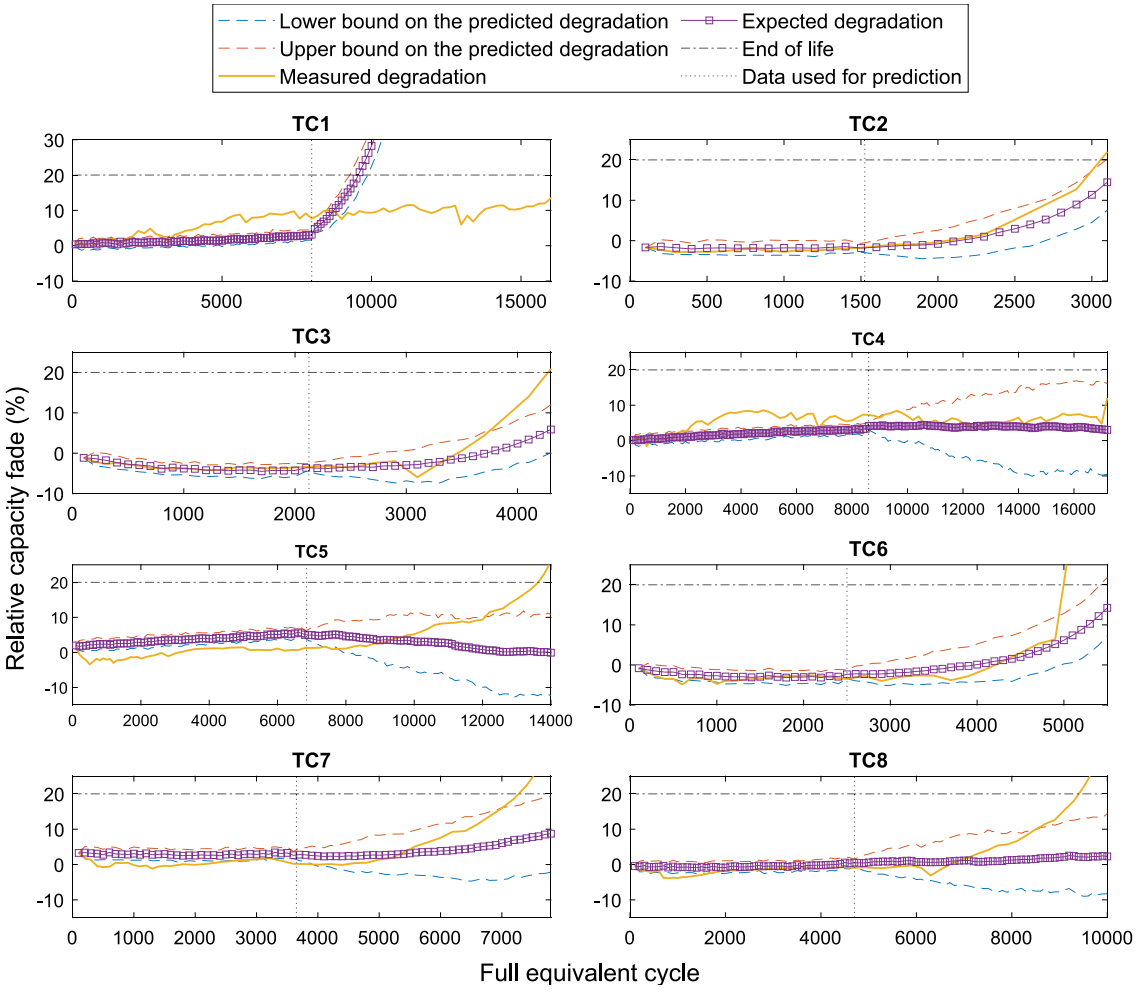

Fig. 18. The predicted capacity fade as a function of FEC, with the existence of 50 % experimental results used for each test-case.

to 12. As can be seen, the lifetime decreases as the temperature increases. As shown in Fig. 10, the cell has a 70 % longer cycle life at 42.5 °C than at 50 °C. In this test condition, the capacity increase phase explained in Section 3.1.2 is not observed. Fig. 11 shows that the cells cycled at 42.5 °C have a 65 % longer cycle life than the cells aged at 50 °C. The result for the low cycle depth test profile is shown in Fig. 12. From this figure, it can be seen that the cells cycled at 42.5 °C have a 2 % lower capacity compared to the 50 °C cells.

4. Lifetime model

The objective of lifetime model development is to estimate the capacity loss of a cell in different applications and predict the expected lifetime as a function of time, or FEC. The target application may have a different profile than the one used for modelling, so a comprehensive model is needed to cover a wide range of applications. In this research, a cyclic ageing model is developed that incorporates the theoretical boundaries summarised in Table 4.

4.1. Capacity fade model

The lifetime model in this research consists of a capacity fade model. The relative capacity fade as a function of FEC for different test-cases given in Table 2 is shown in Fig. 13. The capacity fade trend will be modelled using (3).

$$Normalised\ capacity = \alpha + \beta exp\left(-\gamma|FEC-\eta|^2\right) + \varepsilon \tag{3}$$

where the parameters α, β, γ, and η, are all dependent on the stress-factors (i.e. cycle depth, temperature, and current rate), and ε is noise component with mean zero and constant variance. Due to the complex dependence between the stress factors and the parameters, an FFNN is used to account for this dependence. The FFNN structure was chosen because it offers a good trade-off between generalisation and a relatively fast learning rate compared to more complex neural network structures [31].

The general structure of an FFNN can be seen in the dependent diagram shown in Fig. 14. It relates the input, i.e., cycle depth, C-rate, temperature, and FEC, to the fade in capacity. The input is passed through a series of hidden layers, each consisting of a number of neurons. The information passed to each neuron, indicated by the arrows in the graph, acts as a type of automatic non-linear feature extraction. The general structure of a neuron is shown in Fig. 15, and the neuron of the i^{th} neuron of the j^{th} hidden layer is governed by the Eq. (4).

$$h_{ij} = a\left(\sum_{k=1}^{N_{j-1}} w_{ik}\cdot h_{k(j-1)}\right) \tag{4}$$

where $h_{k(j-1)}$ is k^{th} neuron of the $(j-1)^{th}$ hidden layer, w_{ik} is the weight associated with this dependence (indicated by the arrow between the $h_{k(j-1)}$ and h_{ij}), N_{j-1} is the number of neurons in the $(j-1)^{th}$ layer, and a is an activation function (Note: by the necessity of the notation the zero'th hidden layer is the input layer).

Two FFNNs were used in this paper, the first accounts for the relationship between the parameters and the stress factors seen in (3), while

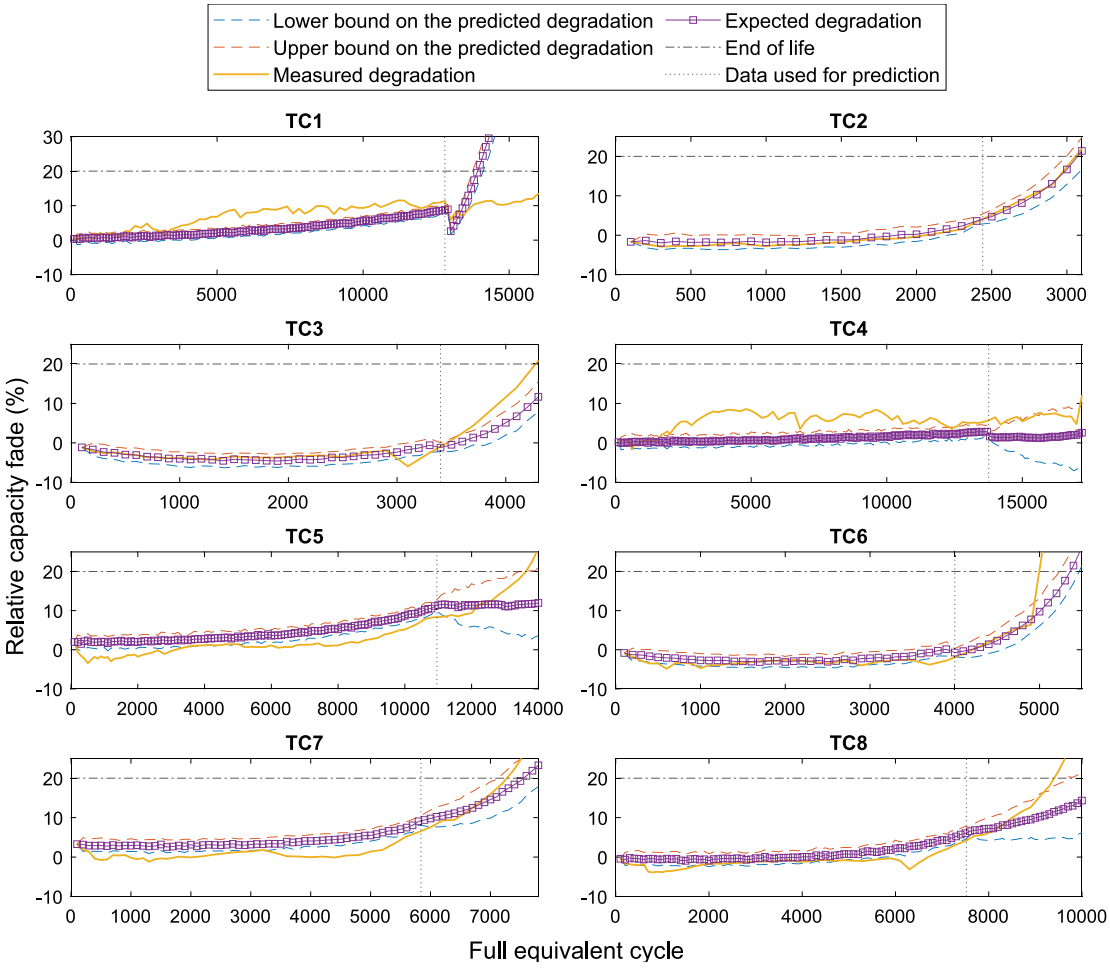

Fig. 19. The predicted capacity fade as a function of FEC, with the existence of 80 % experimental results used for each test-case.

the second FFNN is used to model the residual between the predicted normalised capacity found using the first FFNN and the measured capacity. That is, the second FFNN takes the stress-factors and FEC as an input and aims to model the error between the first FFNN and the measured capacity. The first FFNN uses a single hidden layer with 12 neurons while the second consists of three hidden layers with 36, 24, and 12 neurons, respectively. The activation function used between the hidden layers is an exponential linear unit (ELU). The activation function between the last hidden layer and the output layer is the identity function (also referred to as a linear activation). Using these structures, the weights of the FFNN's were trained using stochastic gradient descent with a Nesterov momentum of 0.9 for 2000 epochs.

The result of training for test-case number 2 can be seen in Fig. 16, which shows the measured and predicted behaviour of this test-case sample used for training.

4.2. Model validation

For validation purposes, each test-case is excluded in turn and the training is performed on the remaining seven test-cases. Furthermore, to assess the sensitivity of the predicted capacity fade on the test-case used for validation, four scenarios are investigated: (1) using no data from the validation test-case during training, (2) using the first 50 % of the data from the validation test-case, (3) using the first 80 % of the data from validation test-case, and (4) using the first 95 % of the data from validation test-case. In order to ascertain the uncertainty in the predicted capacity fade, the FFNN is bootstrapped. That is, 100 bootstrap samples are created (samples of the same size as the original training data created by sampling observations from the original data with replacement) and an FFNN is trained for each of these samples. Using these 100 bootstrapped models, a 95 % confidence envelope is calculated, indicating 95 % of the models yield predictions within these bounds.

The first scenario, assuming that there is no test data for the validation test-case, implies the model must predict the capacity fade for the entire lifetime of the cell. The results using each cell as validation in turn are shown in Fig. 17. The figure shows that in the absence of any data for a given set of stress factors, the predicted capacity fade is very far away from the measured capacity fade. The second scenario uses 50 % of the available validation data for each of the eight test-cases during model training, and the model intends to predict the remaining capacity fade trend, the results of which can be found in Fig. 18. In this figure, the left side of the vertical dotted line is the prediction result using experimental data for training and the right side is the prediction result without using experimental data for training. The figures show that the model is starting to identify the general trend of each test-case, but that the predicted capacity fade is still not entirely in line with the measured capacity fade. The further away from the first 50 % of the test-case data, the better the predictions, except test-case 2. The poor performance is to be expected because few shared stress factors implies that little information is shared in the model. The results of the model predictions for the capacity fade, assuming 80 % existence of the validation data, are shown in Fig. 19. This figure shows that the accuracy of the predicted capacity fade trend increases as more test-case data is added, with test-case 5 being the only test-case where the capacity drop trend was not appropriately captured. This clearly shows that a machine learning based SOH estimation technique is dependent on the existence of data

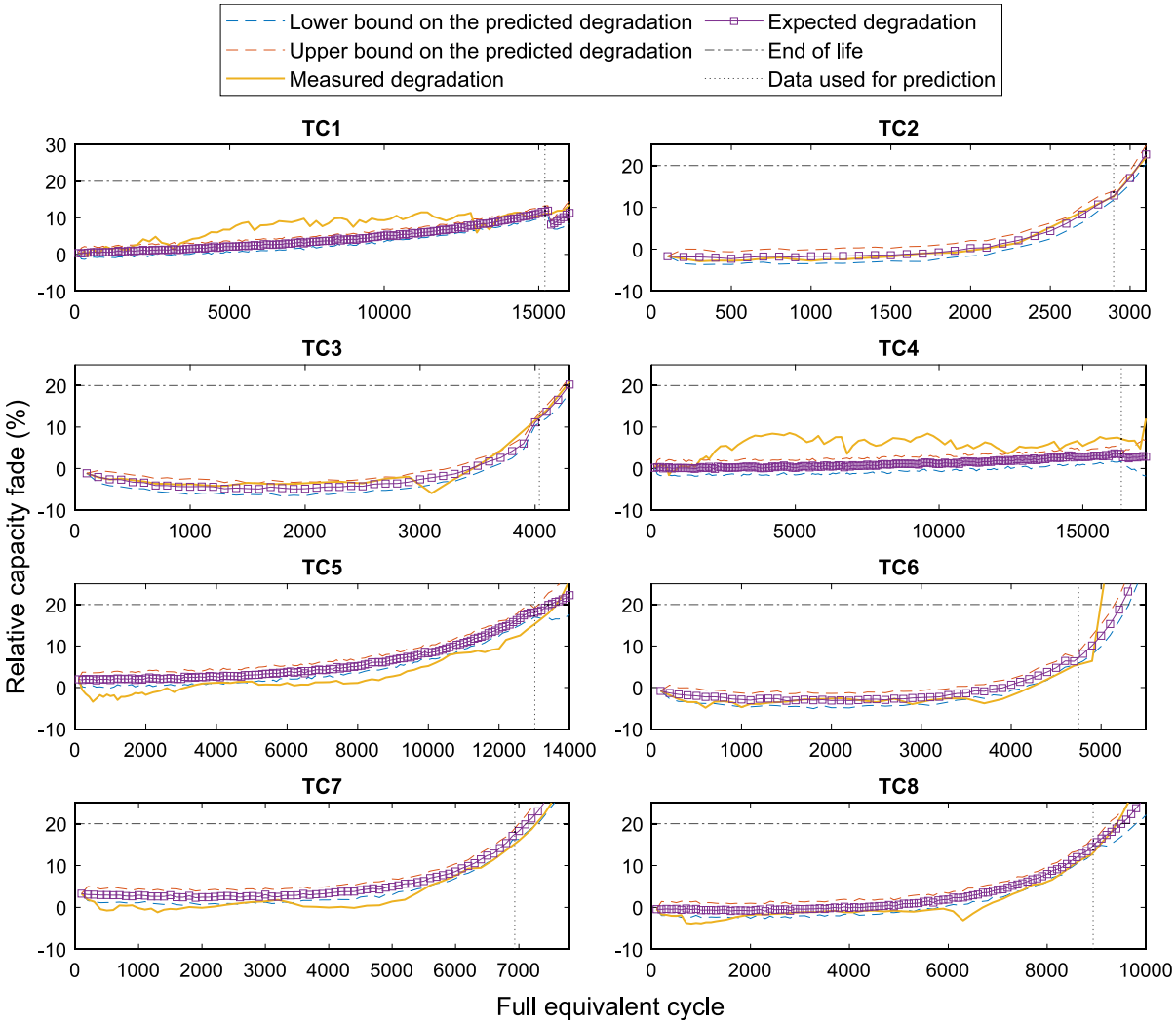

Fig. 20. The predicted capacity fade as a function of FEC, with the existence of 95 % experimental results used for each test-case.

Table 5
Model prediction error at 20 % EOL criterion for test cases in each of the different training scenarios.

Test-case	Measured EOL [FEC]	Predicted EOL [FEC] for each training proportion				Percentage error [%] for each training proportion			
		0 %	50 %	80 %	95 %	0 %	50 %	80 %	95 %
2	3100	–	3243	3127	3099	–	4.61	0.87	0.03
3	4300	–	–	4416	4335	–	–	2.70	0.81
5	13,700	–	–	–	13,500	–	–	–	1.46
6	5000	–	6500	5362	5295	–	30.00	7.24	5.90
7	7300	–	–	7600	7224	–	–	4.11	1.04
8	9500	–	–	10,100	9612	–	–	6.32	1.18

that is very close to the factor of interest. Finally, Fig. 20 shows the results of the model using 95 % of the validation data during training. As can be seen from the figure, using this much of the available data from the test-case of interest leads to very good results for the vast majority of test-cases. The EOL can also be found in all test-cases except for 1 and 4; the error results are summarised in Table 5 calculated as in (5).

$$Percentage\ error\ [\%] = \left|\frac{predicted\ EOL – measured\ EOL}{measured\ EOL}\right| \times 100\% \quad (5)$$

Like the figures, the table shows that as the amount of information from the test-case included during the process increases, the difference between the measured and predicted EOL decreases. Furthermore, it shows that test-case 2 (due to its sharing stress factors with other test-cases), has a percentage error of <5 % using just 50 % of the available information from the test-case. While test-case 6 does not even reach a 5 % error using almost all the information.

The accuracy of the proposed model is further validated using the data-sheet information provided by the manufacturer. As shown in Table 1, the expected lifetime at 55 °C is >4000 FEC. The results of using the developed model trained using all test-cases to predict the EOL under this condition are seen in Fig. 21 and summarised in Table 6. While the result shows that the model can predict EOL with acceptable accuracy (205 FEC on average), it should be noted that the cycles reported in the datasheet are generally a conservative estimate, and this result should therefore be viewed with some reservation. However, in the absence of any information it is deemed a worthwhile exercise.

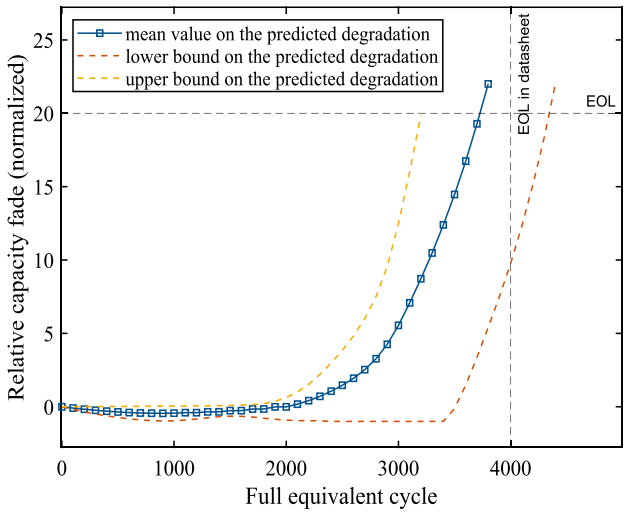

Fig. 21. The predicted EOL as a function of FEC for the test conditions presented by the manufacture.

Table 6
Upper bound, lower bound and mean EOL predicted by the model and its percentage error for the test conditions presented by the manufacturer.

Temperature (°C)	Cycle depth	C-rate	Lower bound [FEC] (percentage error %)	Mean EOL [FEC] (percentage error %)	Upper bound [FEC] (percentage error %)
55	100	2	3200 (20)	3795 (5.13)	4390 (9.75)

5. Conclusion

This paper presents the experimental results obtained from the accelerated ageing test for high power lithium titanate oxide LiBs. The degradation trends as a function of FEC and time in different operating conditions have been presented. The result proves the dependency of the capacity fade on C-rate, temperature, and cycle depth. It was also seen that the longer being imposed to the high temperature in similar test conditions, the shorter cycle life is expected. This paper also presents an accurate SOH estimation and EOL prediction model for LTO cells using a non-linear FFNN. The model has been developed based on a comprehensive experimental result collected in different test conditions covering a variety of stress factors on 16 LTO cells for more than four years. The proposed model was validated using experimental results with a distinct pattern from those used for model training and using the manufacturer's result presented in the datasheet. It proves the ability of the proposed model to predict the EOL and estimate the SOH of the LTO battery in different applications with 5 % accuracy or <250 FEC prediction error.

CRediT authorship contribution statement

Mahdi Soltani: Conceptualization, Methodology, Data Analysis, Writing Original Draft.
Søren B. Vilsen: Writing - Modelling - Review - Editing.
Ana-Irina Stroe: Performing Experiment and Data Collection.
Vaclav Knap: Performing Experiment and Data Collection.
Daniel-Ioan Stroe: Review & Editing.

Declaration of competing interest

The authors declare that they have no known competing financial interests or personal relationships that could have appeared to influence the work reported in this paper.

Data availability

The data that has been used is confidential.

References

[1] C.E. Sandy Thomas, Transportation options in a carbon-constrained world: hybrids, plug-in hybrids, biofuels, fuel cell electric vehicles, and battery electric vehicles, Int. J. Hydrog. Energy 34 (2009) 9279–9296, https://doi.org/10.1016/j.ijhydene.2009.09.058.
[2] V.S. Pallab Barai, Kenneth Higa, Lithium dendrite growth mechanisms in polymer electrolytes and prevention strategies, Phys. Chem. Chem. Phys. (2017), https://doi.org/10.1039/C7CP03304D.
[3] A. Jana, R.E. García, Nano energy lithium dendrite growth mechanisms in liquid electrolytes, Nano Energy 41 (2017) 552–565, https://doi.org/10.1016/j.nanoen.2017.08.056.
[4] M.B. Pinson, M.Z. Bazant, Theory of SEI formation in rechargeable batteries: capacity fade, accelerated aging and lifetime prediction, J. Electrochem. Soc. 160 (2013) A243–A250, https://doi.org/10.1149/2.044302jes.
[5] A. Ghosh, F. Ghamouss, Role of electrolytes in the stability and safety of lithium titanate-based batteries, Front Mater. (2020), https://doi.org/10.3389/fmats.2020.00186.
[6] X.L. Yao, S. Xie, C.H. Chen, Q.S. Wang, J.H. Sun, Y.L. Li, S.X. Lu, Comparisons of Graphite and Spinel Li 1. 33 Ti 1. 67 O 4 as Anode Materials for Rechargeable Lithium-ion Batteries 50, 2005, pp. 4076–4081, https://doi.org/10.1016/j.electacta.2005.01.034.
[7] E.M. Sorensen, S.J. Barry, H. Jung, J.R. Rondinelli, J.T. Vaughey, K. R. Poeppelmeier, N.U. V, E. V, A. V Materials, Three-Dimensionally Ordered Macroporous Li 4 Ti 5 O 12: Effect of Wall Structure on Electrochemical Properties, 2006, pp. 482–489.
[8] Z. Chen, I. Belharouak, Y. Sun, K. Amine, Titanium-Based Anode Materials for Safe Lithium-Ion Batteries, 2012, https://doi.org/10.1002/adfm.201200698.
[9] B. Cui, Advances in spinel Li4Ti5O12 anode materials for lithium-ion batteries, New J. Chem. (2014), https://doi.org/10.1039/C4NJ01390E.
[10] K. Sawai, Y. Iwakoshi, T. Ohzuku, Carbon Materials for Lithium-ion (Shuttlecock) Cells 69, 1994, pp. 273–283.
[11] J.J. Simon Schweidler, Lea de Biasi, Alexander Schiele, Pascal Hartmann, Torsten Brezesinski, Volume changes of graphite anodes revisited: a combined operando X-ray diffraction and in situ pressure analysis study, Phys. Chem. C (2018), https://doi.org/10.1021/acs.jpcc.8b01873.
[12] I. Belharouak, Y.-K. Sun, W. Lu, K. Amine, On the safety of the Li[sub 4]Ti[sub 5]O[sub 12]/LiMn[sub 2]O[sub 4] lithium-ion battery system, J. Electrochem. Soc. 154 (2007) A1083, https://doi.org/10.1149/1.2783770.
[13] X. Hu, L. Xu, X. Lin, M. Pecht, Battery lifetime prognostics, Joule. 4 (2020) 310–346, https://doi.org/10.1016/j.joule.2019.11.018.
[14] W. Vermeer, G.R. Chandra Mouli, P. Bauer, A comprehensive review on the characteristics and modeling of lithium-ion battery aging, in: IEEE Transactions on Transportation Electrification 8, 2022, pp. 2205–2232, https://doi.org/10.1109/TTE.2021.3138357.
[15] S. Bourlot, P. Blanchard, S. Robert, Investigation of aging mechanisms of high power Li-ion cells used for hybrid electric vehicles, J. Power Sources 196 (2011) 6841–6846, https://doi.org/10.1016/j.jpowsour.2010.09.103.
[16] K. Amine, J. Liu, I. Belharouak, S.H. Kang, I. Bloom, D. Vissers, G. Henriksen, Advanced cathode materials for high-power applications, J. Power Sources 146 (2005) 111–115, https://doi.org/10.1016/j.jpowsour.2005.03.227.
[17] M. Soltani, S.H. Beheshti, A comprehensive review of lithium ion capacitor: development, modelling, thermal management and applications, J. Energy Storage (2020), https://doi.org/10.1016/j.est.2020.102019.
[18] M. Soltani, J. Ronsmans, J. Van Mierlo, Cycle life and calendar life model for lithium-ion capacitor technology in a wide temperature range, J. Energy Storage 31 (2020), 101659, https://doi.org/10.1016/j.est.2020.101659.
[19] B. Stiaszny, J.C. Ziegler, E.E. Krauß, M. Zhang, J.P. Schmidt, E. Ivers-Tiffée, Electrochemical characterization and post-mortem analysis of aged LiMn 2O4-NMC/graphite lithium ion batteries part II: calendar aging, J. Power Sources 258 (2014) 61–75, https://doi.org/10.1016/j.jpowsour.2014.02.019.
[20] A.I. Stroe, V. Knap, D.I. Stroe, Comparison of lithium-ion battery performance at beginning-of-life and end-of-life, Microelectron. Reliab. 88–90 (2018) 1251–1255, https://doi.org/10.1016/j.microrel.2018.07.077.
[21] S. Liu, M. Winter, M. Lewerenz, J. Becker, D.U. Sauer, Z. Ma, J. Jiang, Analysis of cyclic aging performance of commercial Li4Ti5O12-based batteries at room temperature, Energy. 173 (2019) 1041–1053, https://doi.org/10.1016/j.energy.2019.02.150.
[22] F. Hall, J. Touzri, S. Wußler, H. Buqa, W.G. Bessler, Experimental investigation of the thermal and cycling behavior of a lithium titanate-based lithium-ion pouch cell, J. Energy Storage 17 (2018) 109–117, https://doi.org/10.1016/j.est.2018.02.012.
[23] T. Nemeth, P. Schröer, M. Kuipers, D.U. Sauer, Lithium titanate oxide battery cells for high-power automotive applications – electro-thermal properties, aging behavior and cost considerations, J Energy Storage 31 (2020), 101656, https://doi.org/10.1016/j.est.2020.101656.
[24] A.I. Stroe, D.L. Stroe, V. Knap, M. Swierczynski, R. Teodorescu, Accelerated lifetime testing of high power lithium titanate oxide batteries, in: 2018 IEEE

Energy Conversion Congress and Exposition, ECCE 2018, 2018, pp. 3857–3863, https://doi.org/10.1109/ECCE.2018.8557416.
[25] T. Bank, J. Feldmann, S. Klamor, S. Bihn, D.U. Sauer, Extensive aging analysis of high-power lithium titanate oxide batteries: impact of the passive electrode effect, J. Power Sources 473 (2020). https://doi.org/https://doi.org/10.1016/j.jpowsour.2020.228566.
[26] A. Chahbaz, F. Meishner, W. Li, C. Ünlübayir, D. Uwe Sauer, Non-invasive identification of calendar and cyclic ageing mechanisms for lithium-titanate-oxide batteries, Energy Storage Mater. 42 (2021) 794–805, https://doi.org/10.1016/j.ensm.2021.08.025.
[27] IEC 62660–-1, Secondary Lithium-ion Cells for the Propulsion of Electric Road Vehicles – Part 1: Performance Testing, 2018.
[28] J. de Hoog, J.M. Timmermans, D. Ioan-Stroe, M. Swierczynski, J. Jaguemont, S. Goutam, N. Omar, J. Van Mierlo, P. Van Den Bossche, Combined cycling and calendar capacity fade modeling of a nickel-manganese-cobalt oxide cell with real-life profile validation, Appl. Energy 200 (2017) 47–61, https://doi.org/10.1016/j.apenergy.2017.05.018.
[29] M. Soltani, J. Ronsmans, J. van Mierlo, Cycle life and calendar life model for lithium-ion capacitor technology in a wide temperature range, J. Energy Storage 31 (2020), https://doi.org/10.1016/j.est.2020.101659.
[30] E. Sarasketa-Zabala, I. Gandiaga, E. Martinez-Laserna, L.M. Rodriguez-Martinez, I. Villarreal, Cycle ageing analysis of a LiFePO4/graphite cell with dynamic model validations: towards realistic lifetime predictions, J. Power Sources 275 (2015) 573–587, https://doi.org/10.1016/j.jpowsour.2014.10.153.
[31] X. Sui, S. He, S.B. Vilsen, J. Meng, R. Teodorescu, D.I. Stroe, A review of non-probabilistic machine learning-based state of health estimation techniques for Lithium-ion battery, Appl. Energy 300 (2021), https://doi.org/10.1016/j.apenergy.2021.117346.